JACS Au
AN OPEN ACCESS JOURNAL OF THE AMERICAN CHEMICAL SOCIETY

pubs.acs.org/jacsau
Article

DNA Logic-Integrated Quantum Nanosensor for MicroRNA Diagnostics

Weiming Lin,[⊥] Tao Ding,[⊥] Die He, Nan Zhang, Haodong Li, Wenjian Luo, Zhongxia Wei, Min Ke, Sisi Jia,* Chunhai Fan, and Le Liang*

Cite This: *JACS Au* 2025, 5, 2123−2134

Read Online

ACCESS | Metrics & More | Article Recommendations | Supporting Information

ABSTRACT: Nanodiamonds (NDs) with nitrogen-vacancy (NV) centers are emerging as powerful quantum nanosensors (QNs) in biomedical applications due to their exceptional sensitivity. However, achieving optimal diagnostics performance necessitates both high sensitivity and selectivity; especially in practical biomedical settings, it remains challenging for QNs to provide quantitative analyses when multiple analytes are present. Here, we present a biosensing platform that integrates DNA logic gates (DLGs) with spin-based quantum sensing, termed DLG-QN for ultrasensitive and ultraselective diagnostics. Utilizing an AND DLG, both NDs and magnetic beads (MBs) are functionalized with hairpin DNA strands. In the presence of both miRNA-21 and miRNA-155—key biomarkers overexpressed in cancer—the hairpin DNAs undergo conformational changes that facilitate DNA-guided self-assembly of NDs and MBs, enriching the target signal. Resonant microwave modulation of ND fluorescence emission allows for high signal-to-noise ratio (SNR) detection by separating the signal from background fluorescence via spin-enhanced analysis. This platform demonstrated ultrasensitive and ultraselective detection of miRNA-21 and miRNA-155 with a limit of detection of 19.8 fM, highlighting its potential as a general biosensing strategy for precision diagnostics involving multiple biomarkers.

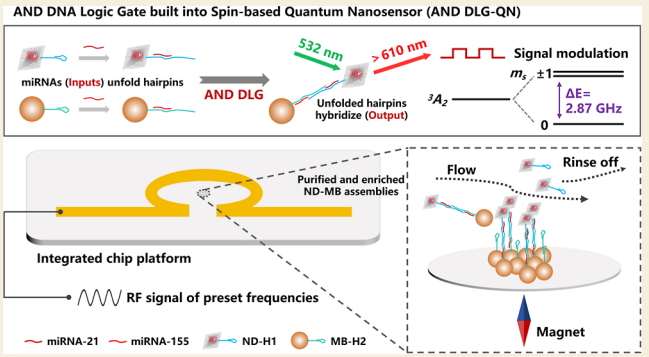

KEYWORDS: *nitrogen-vacancy center, DNA logic gate, spin-enhanced analysis, multiple analytes detection, quantum nanosensor*

1. INTRODUCTION

Nitrogen-vacancy (NV) centers in diamond, functioning as quantum spin systems, exhibit remarkable fluorescence stability and highly controllable optical transitions, making them highly promising qubits in quantum technologies.[1−5] By controlling the transition of energy levels in NV centers from the ground state $m_s = 0$ to the ground states $m_s = \pm 1$, their quantum spin states can be modulated and read out via optically detected magnetic resonance (ODMR) imaging.[6−8] This capability has been leveraged in diverse sensing applications, including magnetic field quantification,[7,9] temperature sensing,[10−12] biological labeling,[13] cellular imaging,[14] and contrast enhancement in magnetic resonance imaging.[15,16] Recent advances have explored spin-enhanced biosensing by modulating the spin states of NV centers for ultrasensitive biomolecule detection.[17] A tailored microwave sequence involving the periodic activation and deactivation of resonant microwave irradiation is applied to NV centers under continuous optical excitation, selectively modulating the NV center fluorescence and effectively separating it from background fluorescence. This spin-based modulation mechanism significantly improves the signal-to-noise ratio (SNR), providing an innovative method for ultrasensitive biomolecule detection.[17,18] In addition, nanodiamonds (NDs) with NV centers, as emerging quantum nanosensors (QNs), are particularly attractive for nanoscale biosensing applications.[19−22] NDs inherit most of the superior properties of bulk diamond and exhibit these properties at the nanoscale, including photostability, biocompatibility, chemical stability, and resistance to harsh environments.[23−27] Moreover, they offer high surface areas and tunable surface chemistries for efficient conjugation with target biomolecules, facilitating specific detection at the nanoscale.[23]

Despite their promise, achieving optimal biosensing performance requires both high sensitivity and high selectivity.[28,29] In practical biomedical applications, especially in complex biological fluids, it remains challenging for QNs to provide reliable quantitative results when multiple analytes are present due to limited selectivity.[28] Biomolecular logic gates

Received: January 16, 2025
Revised: April 19, 2025
Accepted: April 22, 2025
Published: May 12, 2025

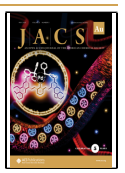

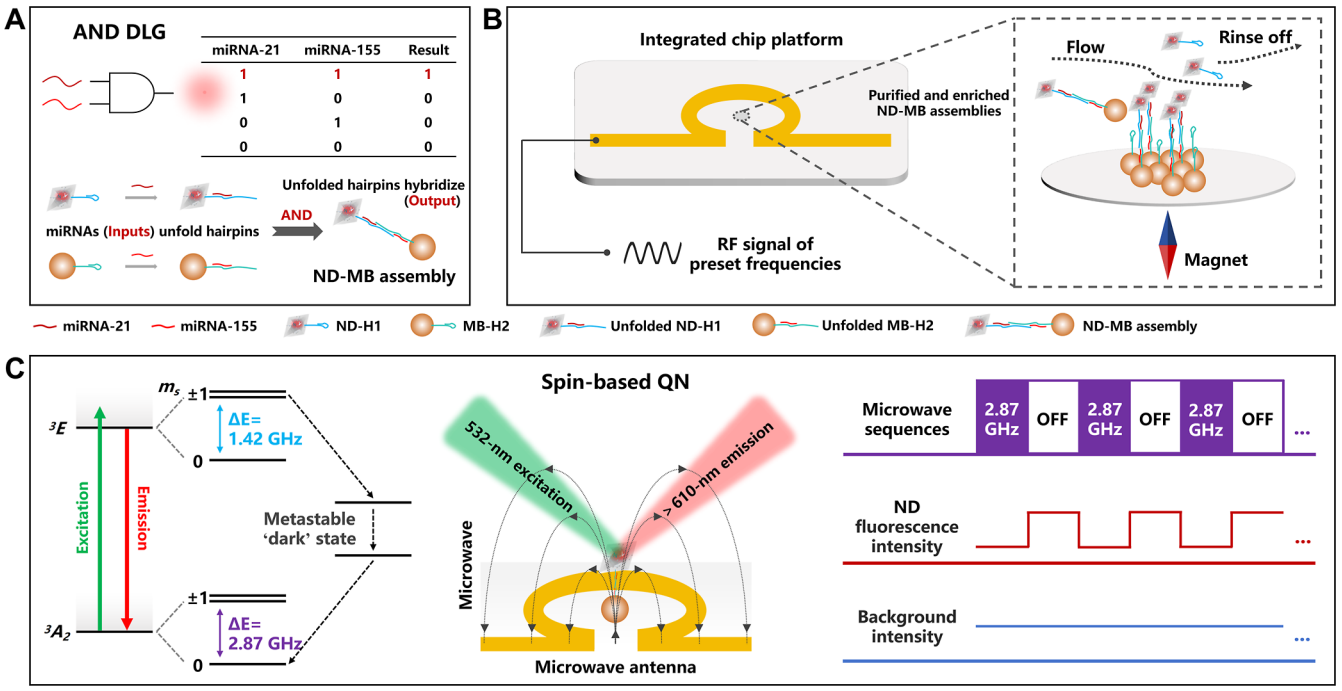

Figure 1. Schematic of the AND DLG-QN platform. (A) AND DLG. Self-assembly between ND-H1 and MB-H2 occurs exclusively in the presence of both miRNA-21 and miRNA-155. (B) Integrated chip platform for imaging and spin manipulation of AND DLG-QN, featuring an omega-shaped microwave antenna that converts preset RF signals into microwaves. (C) Spin-based QN. Left, simplified energy-level diagram and the effect of resonant microwave (i.e., 2.87 GHz) on energy levels of the NV center. Middle, omega-shaped microwave antenna applies a focused and uniform microwave field over the ND-MB assemblies, modulating the fluorescence emission of NV centers within NDs. Right, microwave sequences of preset frequencies selectively modulate the fluorescence emission of NV centers, enabling specific separation of ND fluorescence from background to highly improve the SNR.

offer a solution to enhance selectivity by receiving and integrating multiple biochemical stimuli to generate a definitive output, which is essential for advanced diagnostics that demand handling complex factors with precise control.[30−32] DNA, with its programmability and strict base-pairing rules, serves as an excellent material for constructing such molecular logic gates.[33−38] Importantly, DNA can be easily engineered with different molecules or moieties to selectively bind to various targets (e.g., small molecules, proteins, and nanoparticles), facilitating highly specific labeling systems.[39−45] Incorporating DNA logic gates (DLGs) into biosensing platforms can significantly enhance sensing selectivity, enabling rapid and precise identification of various target molecules via simple logical operations (e.g., AND logic gate),[46,47] thereby substantially improving response efficiency while reducing false-positive rates.

Herein, we established an AND molecular logic gate-based NV sensing system, termed AND DNA Logic Gate built into Spin-based Quantum Nanosensor (AND DLG-QN), aiming for ultrasensitive and ultraselective diagnostics. As a proof of concept, we focus on simultaneous detection of miRNA-21 and miRNA-155, both of which are overexpressed in various cancers and serve as important biomarkers for diagnosis and prognosis.[48−54] Relying on a single biomarker can be problematic due to natural biological variability, individual differences, and potential interference from nondisease-related factors—all of which can lead to false positives or negatives.[55−57] By employing an AND logic gate to require the simultaneous detection of both miRNA-21 and miRNA-155 at clinically relevant levels, our system sets a much stricter diagnostic criterion. This dual detection strategy significantly reduces the likelihood of misdiagnosis because the probability that both biomarkers are erroneously expressed or suppressed in the same sample is considerably lower than that for a single biomarker. Consequently, this approach enhances diagnostic specificity, minimizes false outcomes, and improves the overall accuracy, reliability, and robustness of the clinical diagnostic method. By employing an AND logic gate mechanism, we functionalized NDs and magnetic beads (MBs) with specific hairpin DNA probes that respond to the presence of both miRNA targets. The presence of both miRNA-21 and miRNA-155 as inputs induces conformational changes in the hairpin structures, facilitating the self-assembly of NDs and MBs as the output. These assemblies are further magnetically enriched on the chip surface via a magnet to enhance the imaging signal.

Furthermore, we utilized a microwave field to modulate the fluorescence emission of NV centers in the ND-MB assemblies. This spin-based modulation allows us to separate the specific signal from background fluorescence through frequency-domain analysis, significantly improving the SNR.[17,18] By focusing on this quantum sensing approach, we demonstrate ultraselective and ultrasensitive detection of miRNA-21 and miRNA-155. The integration of DLGs with QNs not only overcomes the selectivity challenge in complex biological matrices but also extends the potential clinical applications of spin-based quantum sensing strategies in biomedical diagnostics.

2. RESULTS AND DISCUSSION

2.1. Design of the AND DLG-QN

To implement the AND DLG, we synthesized hairpin DNA-functionalized NDs (ND-H1) and MBs (MB-H2). The hairpin

https://doi.org/10.1021/jacsau.5c00058
JACS Au 2025, 5, 2123−2134

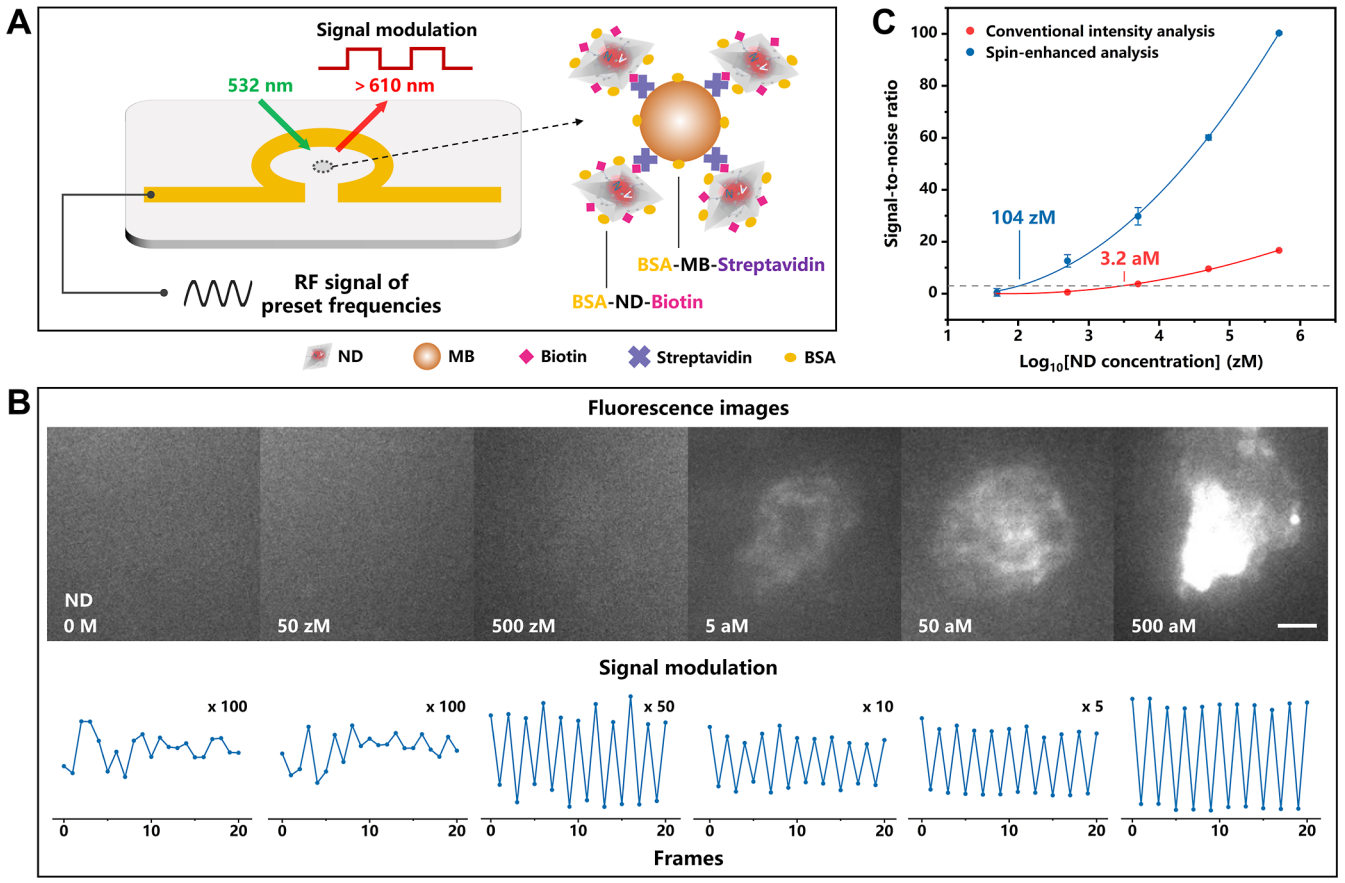

Figure 2. Evaluating the fundamental sensitivity using biotin−streptavidin binding of NDs and MBs. (A) Schematic of the assay. Reaction of BSA-ND-Biotin and BSA-MB-Streptavidin was performed, and purified assemblies were highly enriched by a conical magnet with a sharp tip. (B) Comparison between conventional intensity analysis and spin-enhanced analysis. Top, fluorescence images at various ND concentrations (scale bar: 10 μm); bottom, intensity−frame plots, showing that a periodic signal is still evident after the fluorescent signal is no longer clearly visible in the images. (C) The SNRs of a dilution series of NDs were measured by both conventional intensity and spin-enhanced analyses. LODs were 3.2 aM and 104 zM, respectively. Spin-enhanced analysis provided a ∼30-fold improved sensitivity over conventional intensity analysis. Data are represented as mean ± s.d., where error bars represent the s.d. of n = 20 technical replicates and n = 3 measurement replicates for each sample.

DNA probes are designed to open in the presence of their respective target miRNAs (Figure 1A). In the presence of both miRNA-21 and miRNA-155, the hairpin structures unfold, allowing complementary sequences on ND-H1 and MB-H2 to hybridize and self-assemble. This DNA-guided self-assembly brings the NDs and MBs into close proximity, forming ND-MB assemblies that can be magnetically purified and enriched. Furthermore, we developed an integrated chip platform for imaging and spin manipulation of the DLG-QN system (Figure 1B). Purified ND-MB assemblies are magnetically enriched on the chip surface via a conical magnet with a sharp tip for imaging and analysis. The platform features an omega-shaped microwave antenna that converts preset radio frequency (RF) signals into a focused and uniform microwave field over the measurement area. This design aligns with previous findings, where an omega-shaped stripline resonator was demonstrated to generate a well-confined and uniform peak field.[17]

Conventional intensity and spin-enhanced analyses are employed on the NV centers in the ND-MB assemblies. For spin-enhanced analysis, the NV centers have spin states that can be manipulated using microwave irradiation at a resonant frequency of 2.87 GHz (Figure 1C, left). Specifically, transitions from the ground state m_s = 0 to the ground states m_s = ±1 can be induced by resonant microwave irradiation.[17,19] During the optical excitation and decay, the m_s = ±1 excited-state levels exhibit a higher propensity for decaying into a metastable "dark" state, leading to a reduction in fluorescence emission.[7,17] Consequently, under continuous optical excitation, the NV centers emit fluorescence that can be precisely modulated via a microwave field.

By tailoring a microwave sequence that involves periodic activation and deactivation of resonant microwave irradiation, we induce periodic fluctuations in the fluorescence emission of NV centers under 532 nm laser illumination (Figure 1C, middle and right). This modulation allows us to perform spin-enhanced analysis to separate the specific signal from background fluorescence arising from endogenous biomolecules, buffer solutions, and surface impurities, thus highly improving the SNR. The use of a narrowband resonator integrated on a glass chip (i.e., microwave antenna chip, Figure S1) is well-suited for point-of-care devices as it ensures efficient modulation with low power consumption, making it ideal for such applications.

2.2. Fundamental Sensitivity Limits of the ND-MB System

To assess the fundamental sensitivity limits of our ND-MB system, we employed a high-affinity interaction model (i.e., biotin−streptavidin interaction; Figure 2A). Bovine serum albumin (BSA) coated biotin-functionalized NDs (BSA-ND-

https://doi.org/10.1021/jacsau.5c00058
JACS Au 2025, 5, 2123−2134

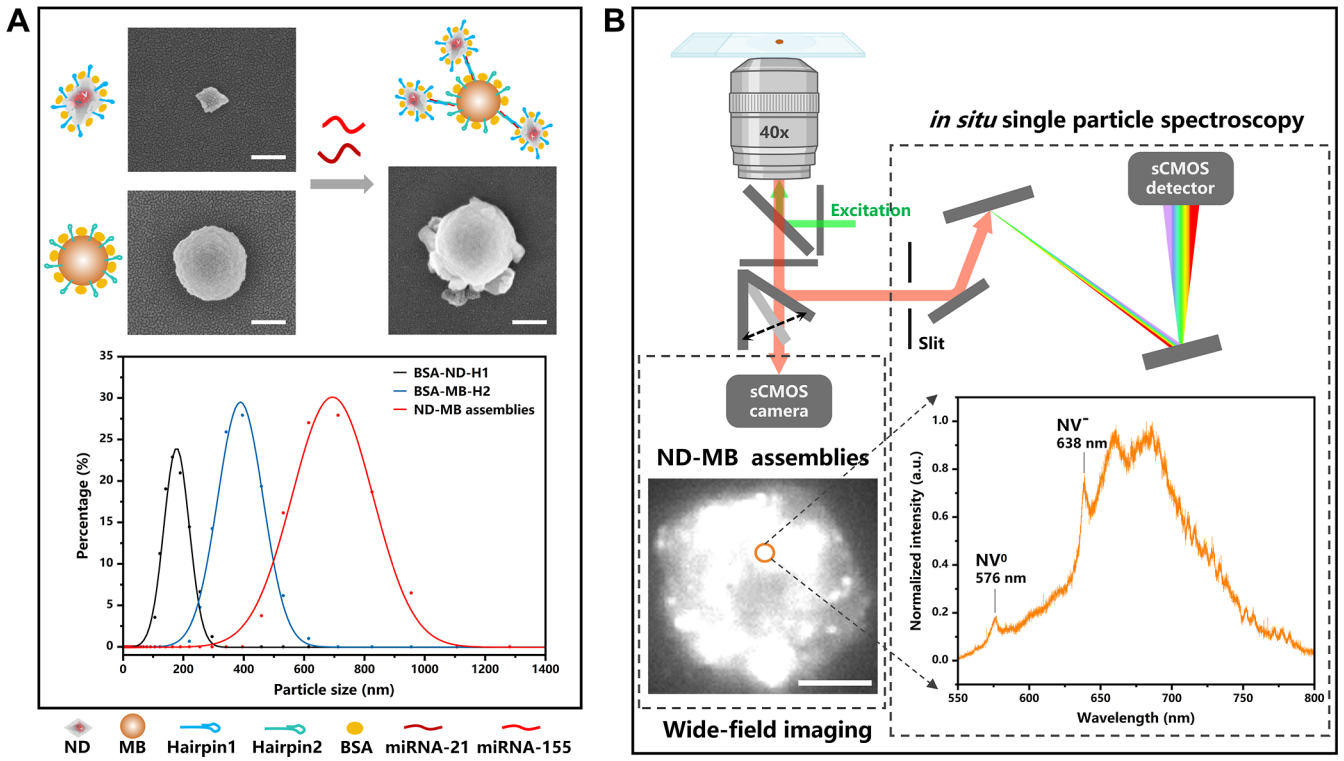

Figure 3. Construction of the AND DLG-QN. (A) SEM images (scale bar: 200 nm) and size distribution plots of BSA-ND-H1, BSA-MB-H2, and ND-MB assemblies. Curves in size distribution plots represent the Gaussian fitting results. (B) Schematic of wide-field imaging and in situ single particle spectroscopy. Typical fluorescence image (scale bar: 10 μm) and emission spectrum of selected ND-MB particles, indicating the photoluminescence (PL) feature of NDs within the assemblies, with zero-phonon lines at 576 and 638 nm for the NV^0 and NV^- centers, respectively.

Biotin) and streptavidin-functionalized MBs (BSA-MB-Streptavidin) were prepared, with the BSA layers employed to minimize nonspecific binding. Additionally, highly efficient purification and enrichment capabilities enabled by magnetic separation provide an ideal scenario for benchmarking sensitivity.

We analyzed the fluorescence signals from all ND-MB assemblies using both conventional intensity and spin-enhanced analyses. A dilution series of NDs was reacted with appropriate amounts of MBs to form ND-MB assemblies. Figure 2B presents fluorescence images of the purified assemblies as well as intensity-frame plots of signal modulation at each ND concentration. These results demonstrate that the periodicity of signal modulation remains evident even after the fluorescent signal is no longer clearly visible through conventional intensity analysis. The SNRs were plotted against ND concentrations (Figure 2C), with each dilution series of NDs fitted to a second-order polynomial to determine the limit of detection (LOD) based on an SNR of 3. The LODs of ND for conventional intensity analysis and spin-enhanced analysis were found to be 3.2 aM and 104 zM, respectively, demonstrating that spin-enhanced analysis provides an ∼30-fold improved sensitivity over conventional intensity analysis.

This fundamental LOD of 104 zM achieved through spin-enhanced analysis corresponds to approximately 0.06 particles per μL or the detection of a single particle in a 16 μL sample. Due to the low numbers of particles detected, the LODs of biological assays are expected to be limited by nonspecific binding and equilibrium considerations rather than by the fundamental sensitivity of spin-based QNs.

To ensure the reliability of spin-based modulation and validate the stability of ND fluorescence, we conducted long-term continuous fluorescence measurement of NDs with 100 measurements taken at 1 s intervals (Figure S2). The fluorescence intensity remained stable throughout the entire measurement period, exhibiting a coefficient of variation of 1.3%. This exceptional photostability of NV centers in NDs can be attributed to the wide bandgap of diamond and the intrinsic stability of the NV^- charge state. The results confirm that signal attenuation due to photobleaching is negligible, reinforcing the robustness of our spin-based detection strategy for extended biosensing applications.

2.3. Construction of the AND DLG-QN

As illustrated in the previous section, a hairpin DNA-based AND DLG was designed. We validated the functionality of the AND DLG through polyacrylamide gel electrophoresis (PAGE), confirming that the hybridization of the hairpin DNAs occurs only in the presence of both miRNA-21 and miRNA-155 (Figure S3). In the absence of either miRNA-21 or miRNA-155, H1 or H2 maintains its closed conformation, precluding the complementary hybridization between them.

Furthermore, ND-H1 and MB-H2 were synthesized for the AND DLG-QN platform. Scanning electron microscopy (SEM) images and size distribution analyses of BSA-ND-H1, BSA-MB-H2, and ND-MB assemblies demonstrated the successful formation of ND-MB assemblies upon the addition of both miRNAs (Figure 3A). More detailed SEM images and size distribution analyses of various synthesized nanoparticles, including ND, ND-H1, BSA-ND-H1, MB, MB-H2, BSA-MB-H2, and ND-MB assemblies, are presented in Figures S4 and

https://doi.org/10.1021/jacsau.5c00058
JACS Au 2025, 5, 2123−2134

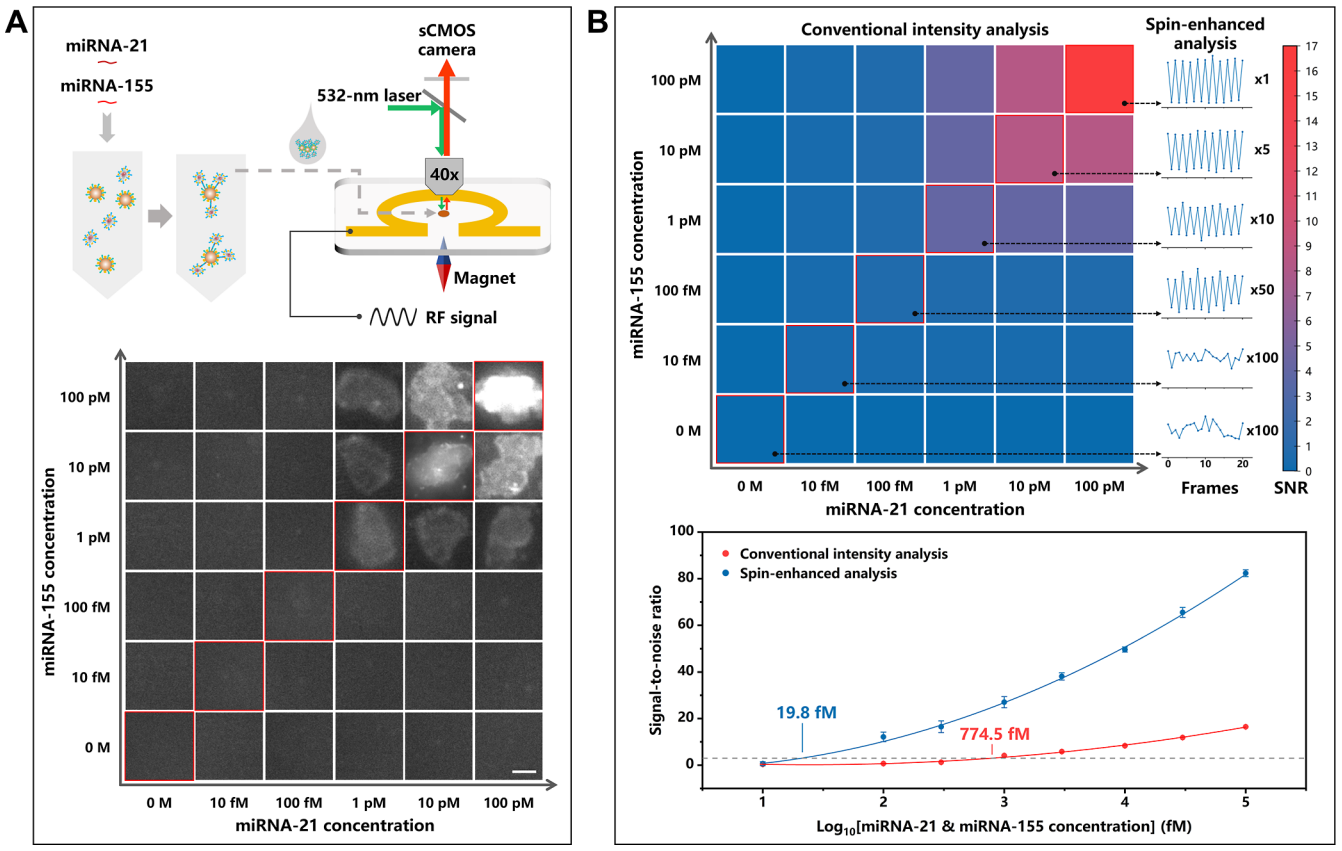

Figure 4. Selectivity and sensitivity of the AND DLG-QN system. (A) Setup and imaging of the AND DLG-QN system. Fluorescence images at various combinations of miRNA-21 and miRNA-155 concentrations (scale bar: 10 μm). (B) Top, two-dimensional color map of SNRs calculated from conventional intensity analysis, and intensity-frame plots derived from spin-enhanced analysis for equal concentrations of miRNA-21 and miRNA-155 (indicated by red-bordered images). Bottom, SNRs for equal concentrations of miRNA-21 and miRNA-155 were measured by both conventional intensity analysis and spin-enhanced analysis. The LODs of AND DLG are 774.5 fM and 19.8 fM, respectively. Spin-enhanced analysis provided a ~40-fold improved sensitivity over conventional intensity analysis. Data are represented as mean ± s.d., where error bars represent the s.d. of n = 20 technical replicates and n = 3 measurement replicates for each sample.

S5. Further, the in situ single particle fluorescence spectroscopy confirmed the presence of NV centers in the ND-MB assemblies enriched by magnetic separation (Figure 3B). The corresponding fluorescence spectrum displayed a broad emission band between 550 and 750 nm, which is characteristic of the spontaneous emission from NDs. The zero-phonon lines at 576 and 638 nm, attributed to the neutral charged state (NV^0) and negatively charged (NV^-) state of the NV center,[3] respectively, were also well discernible. These results collectively demonstrate the successful implementation of AND DLG-QN through the DNA-guided self-assembly of NDs and MBs.

2.4. Selectivity and Sensitivity of the AND DLG-QN System

We evaluate the selectivity and sensitivity of the AND DLG-QN system by testing various concentration combinations of miRNA-21 and miRNA-155, ranging from 10 fM to 100 pM. The obtained fluorescence images for each parameter combination are displayed in Figure 4A. Both conventional intensity analysis and spin-enhanced analysis were employed (Figure 4B, top). The two-dimensional color map of SNRs calculated from conventional intensity analysis intuitively illustrates the excellent selectivity of AND DLG-QN. As illustrated in Figure S6, the statistical analysis of intergroup differences—both among miRNA-155 concentration groups at a constant miRNA-21 concentration of 10 pM and among miRNA-21 concentration groups at a constant miRNA-155 concentration of 10 pM—further validates the superior selectivity of AND DLG-QN. Notably, the intensity-frame plots derived from spin-enhanced analysis for equal concentrations of miRNA-21 and miRNA-155 (indicated by red-bordered images) reveal that a periodic signal remains evident after the fluorescent signal is no longer clearly visible, confirming the functionality of the AND DLG-QN system. Complete fluorescence images and the corresponding conventional intensity analysis and spin-enhanced analysis are presented in Figures S7 and S8, providing a more comprehensive evaluation of the diagnostic performance of the AND DLG-QN system.

The SNRs obtained from conventional intensity analysis and spin-enhanced analysis were plotted against equal concentrations of miRNA-21 and miRNA-155 (Figure 4B, bottom). Each dilution series of miRNA-21 and miRNA-155 was fitted to a second-order polynomial to determine the LOD based on a SNR of 3. The spin-enhanced analysis achieved a LOD of 19.8 fM for the simultaneous detection of miRNA-21 and miRNA-155, which is approximately 40 times more sensitive than the conventional intensity analysis with a LOD of 774.5 fM. The LOD of 19.8 fM achieved by our platform, without the need for nucleic acid amplification, is comparable or superior to other oligonucleotide detection methods (i.e.,

https://doi.org/10.1021/jacsau.5c00058
JACS Au 2025, 5, 2123−2134

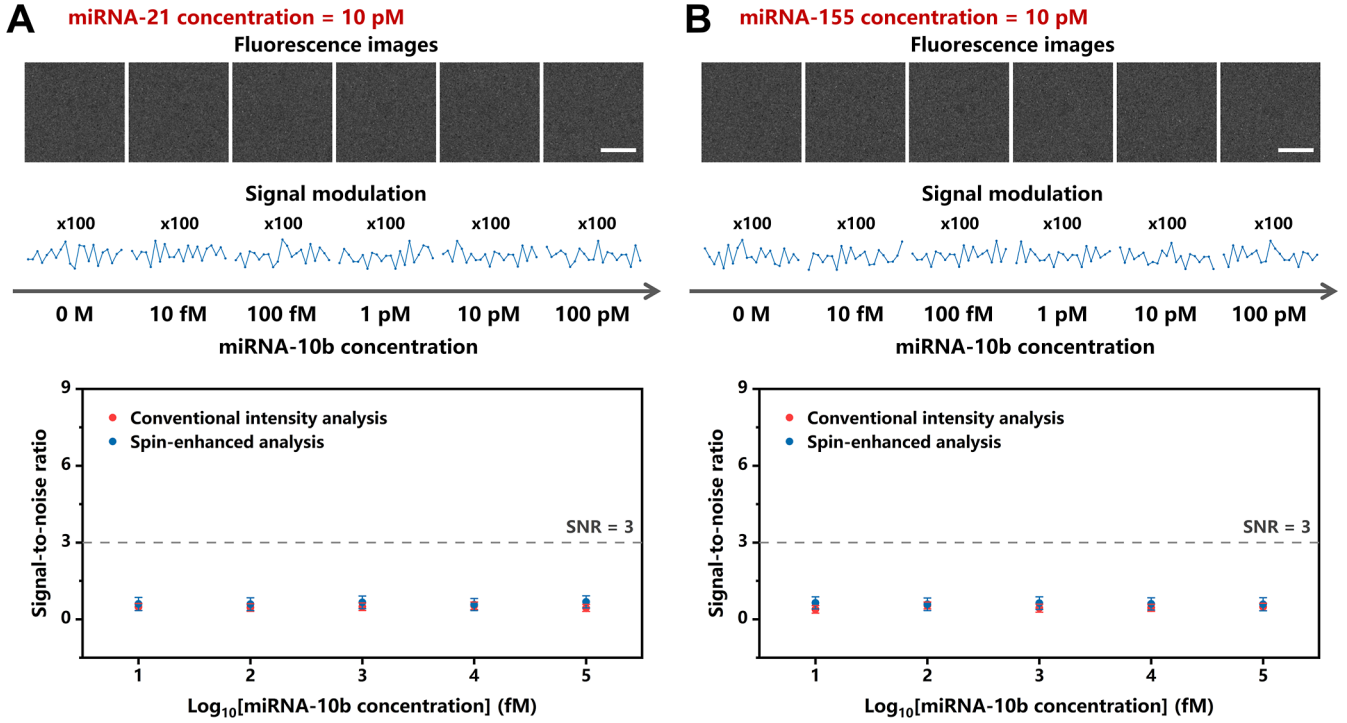

Figure 5. Selectivity of the AND DLG-QN system for detecting specific targets (miRNA-21 and miRNA-155) was evaluated by performing the AND DLG-QN assay under two experimental configurations: (A) 10 pM of miRNA-21 with various concentrations of miRNA-10b and (B) 10 pM of miRNA-155 with various concentrations of miRNA-10b. Top, fluorescence images at various miRNA-10b concentrations (scale bar: 10 μm) and corresponding intensity-frame plots under signal modulation; bottom, the SNRs of various miRNA-10b concentrations were measured by both conventional intensity analysis and spin-enhanced analysis. Data are represented as mean ± s.d., where error bars represent the s.d. of n = 20 technical replicates and n = 3 measurement replicates for each sample.

LODs of 3.7 fM to 670 fM),[17,58−63] as summarized in Table S1.

Moreover, the selectivity of the AND DLG-QN system for detecting specific targets (miRNA-21 and miRNA-155) was evaluated by introducing miRNA-10b as an interference target. The AND DLG-QN assay was performed under two experimental configurations: 10 pM miRNA-21 with various concentrations of miRNA-10b (Figure 5A) and 10 pM miRNA-155 with various concentrations of miRNA-10b (Figure 5B). SNRs obtained from conventional intensity and spin-enhanced analyses for both experimental configurations were substantially below the detection threshold (SNR = 3). The absence of detectable cross-reactivity with similar miRNAs underscores the exceptional specificity of the designed AND DLG toward miRNA-21 and miRNA-155.

Collectively, these results demonstrate that the developed AND DLG-QN platform exhibits outstanding selectivity and sensitivity in detecting the target biomarkers miRNA-21 and miRNA-155. This superior performance can be attributed to the meticulously engineered design of AND DLG, the efficient purification and enrichment capabilities of ND-MB assemblies, and the implementation of a spin-based quantum sensing strategy.

2.5. Clinical Applicability of the AND DLG-QN

The AND DLG-QN has exhibited exceptional selectivity and sensitivity in detecting miRNA-21 and miRNA-155, and we strive to expand the AND DLG-QN in complex biological matrices. Unlike the well-known buffers with well-defined components, biological samples introduce challenges due to the presence of substantial biomolecules that may interfere with the accurate quantification of multiple biomarkers. To demonstrate the performance of AND DLG-QN under more clinically relevant conditions, we performed recovery assays in serum samples spiked with known concentrations of miRNA-21 and miRNA-155 (100 fM to 100 pM) and followed by spin-enhanced analysis of AND DLG-QN (Figure 6A).

As shown in Figure 6B, the measured concentrations of miRNA-21 and miRNA-155 correlated well with the added amounts, with a correlation coefficient (R^2) of 0.9895. The recovery rates, determined by the ratio of the measured concentration to the added concentration, ranged from 92.3% to 103.3% (Figure 6B and Table 1). These results demonstrate that our platform maintains its selectivity and sensitivity and exhibits satisfactory clinical applicability for analyzing miRNA-21 and miRNA-155 in complex biological matrices, highlighting its potential for clinical diagnostics.

3. CONCLUSIONS

We have advanced precision diagnostics by integrating DLGs with QNs, leveraging the exceptional sensitivity of NV centers in NDs alongside the high selectivity afforded by DNA-based AND logic operations. Additionally, the DNA-guided self-assembly of NDs and MBs amplifies signal strength and allows for magnetic separation, enhancing detection sensitivity in complex biological samples such as serum. This approach addresses common challenges in biosensing, such as non-specific interactions and background interference, highlighting the clinical potential of this platform for early cancer diagnostics.

Despite these promising results, several aspects warrant further investigation. Although the AND logic gate significantly improves diagnostic specificity by ensuring that only samples

https://doi.org/10.1021/jacsau.5c00058
JACS Au 2025, 5, 2123−2134

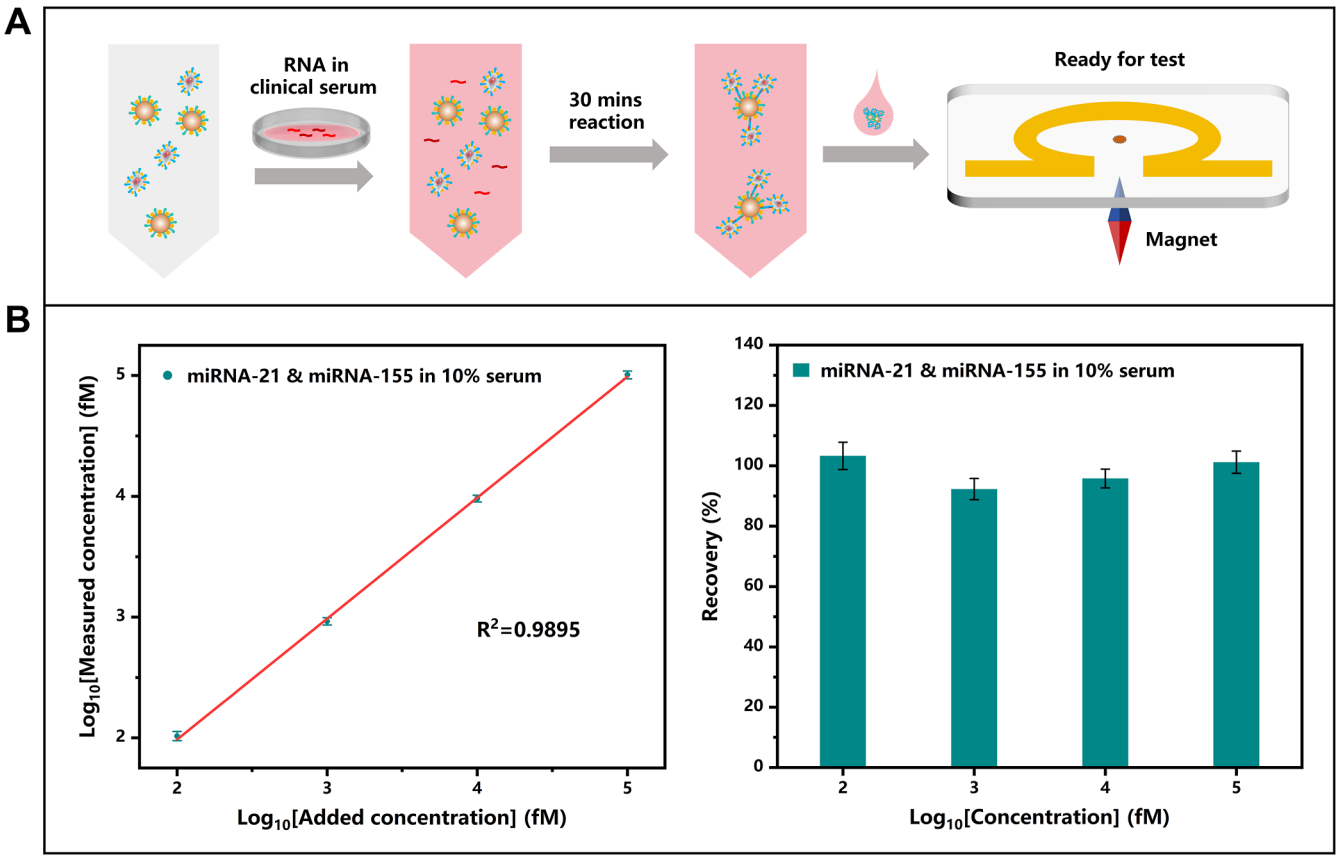

Figure 6. Clinical applicability of the AND DLG-QN. (A) Schematic workflow of the recovery assay. Determination of miRNA-21 and miRNA-155 spiked into clinical serum using spin-enhanced analysis of AND DLG-QN. (B) Left, correlation between the measured and added concentrations of miRNA-21 and miRNA-155 in 10% serum, with a R^2 of 0.9895. Right, recovery assay results of miRNA-21 and miRNA-155 spiked into 10% serum. Recovery rates were determined by the ratio of the measured concentration to the added concentration. Data are represented as mean ± s.d., where error bars represent the s.d. of n = 20 technical replicates and n = 3 measurement replicates for each sample.

Table 1. Determination of miRNA-21 and miRNA-155 Spiked into Clinical Serum Using Spin-Enhanced Analysis of AND DLG-QN

added	measured	recovery (%)	RSD (%)
100 fM	103.33 fM	103.3	4.5
1 pM	0.92 pM	92.3	3.5
10 pM	9.58 pM	95.8	3.1
100 pM	101.24 pM	101.2	3.7

with both miRNA-21 and miRNA-155 above the clinical threshold produce a detectable signal, it does not provide separate quantitative information for each biomarker. In future iterations, by incorporation of additional techniques such as multiplexed fluorescent readout strategies or orthogonal quantification assays, the DLG-QN can independently quantify each biomarker while still benefiting from the enhanced selectivity offered by the AND logic gate. This combined approach would allow for both high specificity and accurate quantification of each target, thereby providing a more comprehensive diagnostic tool. Additionally, while the current platform was tested using specific miRNAs associated with cancer, expanding the range of detectable biomarkers could significantly enhance its utility across various diseases. The versatility of DNA logic gates enables opportunities to expand the platform's capabilities beyond the detection of miRNA-21 and miRNA-155. This approach is inherently adaptable to other miRNA combinations. The modular and programmable nature of DNA logic gates allows for straightforward modification of hairpin DNA sequences to recognize different miRNA targets, extending the platform's applicability to a broader spectrum of biomarkers relevant to various diseases. By designing different logic gate configurations (e.g., OR, NAND, and NOR) and incorporating diverse DNA sequences, we can tailor the system to detect a broader array of biomarkers linked to various diseases. Furthermore, the potential for multiplexed detection enables simultaneous analysis of multiple miRNA targets, further enhancing the platform's capability in complex biological environments. This flexibility is particularly valuable in the context of precision medicine, where personalized diagnostic tools are essential for effective patient management.

In conclusion, the AND DLG-QN platform presents a versatile and powerful tool for the simultaneous detection of multiple biomarkers with exceptional sensitivity and selectivity. Future work should focus on broadening the spectrum of detectable analytes and improving the system's practicality, paving the way for its integration into clinical diagnostics to advance precision medicine.

4. EXPERIMENTAL SECTION

4.1. Materials and Reagents

Biotinylated fluorescent NDs (1 nM, 100 nm in diameter) were purchased from Adamas Nanotechnologies (USA). Streptavidin MBs (10 mg mL^{-1}, 300 nm in diameter) and carboxylated MBs (10 mg

https://doi.org/10.1021/jacsau.5c00058
JACS Au 2025, 5, 2123−2134

mL^{-1}, 300 nm in diameter) were purchased from Beaver Biomedical Engineering (China). MES buffer (100 mM, pH 6.0) and Tween-20 were purchased from Yuanye Biotechnology (China). Streptavidin, BSA, and 1-(3-dimethylaminopropyl)-3-ethylcarbodiimide hydrochloride (EDC) were purchased from Aladdin Biochemical Technology (China). Tris−HCl buffer (1 M, PH 8.0) was purchased from Solarbio Technology (China). Ethylene diamine tetraacetic acid (EDTA), TBE buffer, and ammonium persulfate (APS) were purchased from Macklin Biochemical Technology (China). TAE buffer, SSC buffer, *N*,*N*,*N*′,*N*′-tetramethylethylenediamine (TEMED), and BeyoRed DNA loading buffer (6×) were purchased from Beyotime Biotechnology (China). Acrylamide was purchased from Meryer Biochemical Technology (China). ExRed nucleic acid electrophoresis dye (10,000×) was purchased from Zoman Biotechnology (China). Sodium chloride (NaCl) was purchased from Energy Chemical (China). Positive photoresist (AZ 5214) and its developer (AZ 300MIF) were purchased from MicroChem Co. (USA). Acetone, anhydrous ethanol, iodine, potassium iodide, 36% concentrated hydrochloric acid, *N*-methylpyrrolidone, and isopropyl alcohol were purchased from Sinopharm Chemical Reagent (China). All oligonucleotides were synthesized by Sangon Biotech (China), and the specific sequences are listed in Table S2. Ultrapure water (18.2 MΩ cm at 25 °C) produced by a Millipore purification system (Milli-Q IQ Element, Merck, USA) was used throughout our experiments.

4.2. Polyacrylamide Gel Electrophoresis

The polyacrylamide gel was prepared by mixing 6 mL of 30% acrylamide solution, 3.5 mL of ultrapure water, 2.4 mL of 5× TBE buffer, 100 μL of 10% APS, and 8 μL of TEMED. The mixture was allowed to polymerize in a casting frame. The nucleic acid staining solution was prepared by mixing 15 μL of ExRed nucleic acid electrophoresis dye (10,000×), 5 mL of 1 M NaCl solution, and 45 mL of ultrapure water. The hairpin DNAs were annealed at 95 °C for 10 min and cooled to room temperature (RT).

Each nucleic acid reaction mixture was incubated in 1× SSC buffer at RT for 40 min and then mixed with BeyoRed DNA loading buffer. The samples were then loaded onto a prepared polyacrylamide gel (10 μL per lane) and subjected to electrophoresis in 1× TBE buffer at 90 V for 80 min. After electrophoresis, the gel was stained with the prepared nucleic acid staining solution, followed by photography under UV light using a Gel Imaging analysis system (ZF-288, JIAPENG, China).

4.3. Preparation of ND-H1

200 μL portion of biotinylated NDs (1 nM) was mixed with 25 μL of streptavidin (20 μM). The total volume was adjusted to 1000 μL with ultrapure water, and the mixture was shaken for 2 h at RT. The complete binding of biotin on the ND surface and streptavidin was followed by centrifugation (2700 rpm for 15 min) to remove free streptavidin. The resultant purified product was mixed with 10 μL of biotinylated hairpin1 (100 μM). The total volume was also adjusted to 1000 μL with ultrapure water, and the mixture was shaken for 2 h at RT. ND-H1 were isolated through three rounds of centrifugation (2700 rpm for 15 min each) with ultrapure water, resulting in a final volume of 200 μL. ND-H1 were then blocked overnight with 2 mL of 1× TAE buffer containing 1% w/v BSA. After overnight blocking, BSA-ND-H1 were purified by three rounds of centrifugation (2100 rpm for 15 min each) with 1× TAE buffer and resuspended in 200 μL of 1× TAE buffer. The concentration of BSA-ND-H1 was 1 nM, and the compounds were stable for ∼2 months at 4 °C.

4.4. Preparation of MB-H2

200 μL of carboxylated MBs (10 mg mL^{-1}) were washed twice with MES buffer (100 mM, pH 6.0) and then resuspended in 20 μL of the MES buffer. 10 μL of EDC (1.6 M) and 10 μL of aminated hairpin2 (100 μM) were then added to the carboxylated MB solution, and the mixture was shaken for 5 h at RT. MB-H2 were isolated through two rounds of magnetic separation with TT buffer (0.01% v/v Tween-20 in 250 mM of Tris−HCl buffer, pH 8.0), followed by two rounds of magnetic separation with 1× TAE buffer, resulting in a final volume of 200 μL. MB-H2 were then blocked overnight with 2 mL of 1× TAE buffer containing 1% w/v BSA. After overnight blocking, BSA-MB-H2 were purified by three rounds of magnetic separation with 1× TAE buffer and resuspended in 200 μL of TE buffer (10 mM of Tris−HCl buffer containing 1 mM of EDTA, pH 8.0). Before the AND DLG assay, BSA-MB-H2 needed to be washed twice with 1× TAE buffer to remove the residual EDTA. The concentration of BSA-MB-H2 was 0.23 nM, and they were stable for ∼2 months at 4 °C.

4.5. Characterization of Nanoparticles

The morphologies of ND series (ND, ND-H1, BSA-ND-H1), MB series (MB, MB-H2, BSA-MB-H2), and ND-MB assemblies were visualized using SEM (Zeiss GeminiSEM 500, Zeiss, Germany) operated at 5 kV.

The size distributions of ND series, MB series, and ND-MB assemblies were determined by using a dynamic light scattering (DLS) instrument (Zetasizer Nano ZSP, Malvern, UK). Measurements were conducted at a detection angle of 173° with a 10 mW He−Ne laser operating at a wavelength of 633 nm for analysis.

4.6. Optical Measurement Setup

Optical measurements were performed at RT under ambient conditions by using a custom-built wide-field imaging and in situ single particle spectroscopy system.

Wide-field imaging: a 532 nm laser (OBIS Laser Box, Coherent Inc., USA) was transmitted through a 532 ± 2 nm band-pass filter and a 532 nm long-pass dichroic mirror to focus on the sample using a 40× objective lens (NA = 0.60). The PL of the sample was separated from the 532 nm laser by the aforementioned dichroic mirror. Then, the PL passed through a 610 nm long-pass filter to reach a back illuminated scientific CMOS (KURO 1200B, Princeton Instruments, USA) for wide-field fluorescence imaging.

In situ single particle spectroscopy: a 532 nm laser (OBIS Laser Box, Coherent Inc., USA) was transmitted through a 532 ± 2 nm band-pass filter and a 532 nm long-pass dichroic mirror to focus on the sample using a 40× objective lens (NA = 0.60). The PL of the sample was separated from the 532 nm laser by the aforementioned dichroic mirror and then passed through a 537 nm long-pass filter. A region of interest (ROI) was manually defined, and the PL from this ROI was directed to a grating spectrometer (SpectraPro HRS-500, Princeton Instruments, USA) equipped with a 600 g/mm grating and a back illuminated scientific CMOS (KURO 1200B, Princeton Instruments, USA) for in situ single particle spectrum measurements.

4.7. Fabrication of the Microwave Antenna Chip

The omega-shaped microwave antenna chip was fabricated via a three-step process:[1] the deposition of a titanium−gold (Ti−Au) bilayer on the borosilicate glass wafer via electron beam evaporation;[2] the fabrication of an omega-shaped photoresist pattern on the wafer via standard maskless lithography; and[3] the fabrication of the wafer deposited with an omega-shaped Ti−Au bilayer (i.e., microwave antenna chip) via wet etching. The detailed fabrication flowchart is shown in Figure S9, and the structural parameters of the omega-shaped microwave antenna are depicted in Figure S10.

First, a 50 nm-thick Ti layer and a 500 nm-thick Au layer were sequentially deposited on the surface of a 500 μm-thick borosilicate glass wafer (BF33, Schott AG, Germany) by electron beam evaporation via an E-beam evaporation system (vapor station 4, Oxford Vacuum Science, UK). Ti layer served as an adhesive layer to ensure the strong adhesion between the Au layer and the wafer. Postdeposition, the wafer was allowed to cool under vacuum to avoid oxidation of the freshly deposited layers. Subsequently, the entire wafer was segmented into smaller wafers of a desirable size via a wafer scribing and cleaving system (LatticeAx 420, Ted Pella, USA). These wafers were then immersed in acetone for 10 min, followed by anhydrous ethanol for 5 min, and finally rinsed with ultrapure water.

To fabricate the omega-shaped pattern, the positive photoresist AZ 5214 was spin-coated onto the wafer deposited with a Ti−Au bilayer at 600 rpm for 5 s and another 4000 rpm for 30 s to deposit a 1.3 μm-thick photoresist coating. The wafer was then baked at 100 °C for 3 min. Subsequently, UV exposure (300 mJ cm^{-2}) was applied to

https://doi.org/10.1021/jacsau.5c00058
JACS Au 2025, 5, 2123−2134

selectively irradiate the photoresist coating on the wafer, excluding the regions corresponding to the desired pattern, via a maskless aligner (MLA150, Heidelberg Instruments, Germany). Afterward, the wafer was developed in AZ 300MIF for 37 s under continuous shaking to dissolve the exposed photoresist. The residual photoresist was washed away in ultrapure water and dried with nitrogen gas. After that, the wafer was heated to 100 °C for 90 s to enhance the stability of the photoresist pattern.

The wafer, deposited with a Ti−Au bilayer and photoresist pattern, was immersed in a solution containing iodine (60 mg mL^{-1}) and potassium iodide (200 mg mL^{-1}) for 20 s to selectively etch the Au layer beyond the photoresist pattern. This was followed by rinsing with ultrapure water and drying with nitrogen gas. Subsequently, the wafer was immersed in 36% concentrated hydrochloric acid for 40 min to selectively etch the Ti layer beyond the photoresist pattern, followed by rinsing with ultrapure water and drying with nitrogen gas. Afterward, the wafer was immersed in *N*-methylpyrrolidone at 60 °C for 30 min and then in acetone for an additional 30 min to remove the photoresist pattern. Finally, the wafer was rinsed with isopropanol and ultrapure water and dried with nitrogen gas, resulting in the fabrication of a wafer deposited with an omega-shaped Ti−Au bilayer (i.e., microwave antenna chip).

4.8. Construction of the Microwave Generating Device

The microwave generating device is constructed from an RF signal source, two RF isolators, a power amplifier, a DC power supply, and a microwave antenna chip. RF signal source (SSG3032X-IQE, Siglent Technologies, China) is employed to produce RF signal sequences at preset frequencies. Power amplifier (ZHL-16W-43-S+, Mini-Circuits, USA) serves to enhance the power of RF signals with a gain of 45 dB, energized by a DC power supply (GPS305D, Wanptek, China). RF isolators (UIYBCI4040A, UIY Inc., China) are integrated to prevent the reflection of electrical signals to protect critical components. The microwave antenna chip is responsible for emitting microwaves at preset frequencies and facilitating their focused and uniform propagation. Schematic of the microwave generating device is shown in Figure S11.

4.9. Resonant Microwave Modulation of ND Fluorescence Emission

An NV^- center accommodates an extra electron, forming a quantum spin triplet ground state with three spin sublevels ($m_s = 0, \pm1$).[2] The ground state $m_s = 0$ can be transitioned to the ground states $m_s = \pm1$ via electron spin resonance induced by microwave irradiation at a resonant frequency of 2.87 GHz.[17,19] Upon optical excitation, the triplet ground state is elevated to an excited triplet state, which subsequently undergoes radiative decay back to the ground state to emit fluorescence. During the process, the $m_s = \pm1$ excited-state levels exhibit a higher propensity for decaying into a metastable "dark" state, leading to a reduction in fluorescence.[7,17] Consequently, resonant microwave irradiation can decrease the fluorescence emission of NV centers by transferring the electron spin population from the ground state $m_s = 0$ to the ground states $m_s = \pm1$.

When a tailored microwave sequence, involving periodic activation and deactivation of resonant microwave irradiation, is applied to NV centers under continuous optical excitation, the resultant fluorescence emission from NV centers exhibits an orderly modulation between low and high intensities. In this study, the microwave power was set to 100 mW, with a cycle period of 2 s, during which the activation and deactivation states each lasted for 1 s. This feature is leveraged to selectively modulate the fluorescence emission of NV centers, enabling the specific separation of ND fluorescence from background fluorescence to highly improve the SNR, which is termed spin-enhanced analysis. Specifically, signal acquisition for spin-enhanced analysis involved 20 technical replicates, during which the amplitude of changes in fluorescence emission from NV centers was measured over 20 cycles, alternating between low and high intensities (including both upward and downward transitions).

4.10. Assay for Biotin−Streptavidin Binding of NDs and MBs

The fundamental LOD of binding between NDs and MBs was investigated by using a model biotin−streptavidin interaction. A serial dilution of BSA-ND-Biotin was reacted with BSA-MB-Streptavidin for 30 min. The BSA blocking layers were employed to minimize nonspecific binding. NDs were directly bound to MBs via the high-affinity interaction between biotin and streptavidin. The reaction products were then subjected to three rounds of magnetic separation to obtain the purified ND-MB assemblies.

The resulting fluorescence signals from the purified ND-MB assemblies were analyzed using conventional intensity analysis and spin-enhanced analysis (described in "4.9"). The SNR of conventional intensity analysis was calculated using formula 1, with the fluorescence intensity of the experimental group as A_{signal} and the fluorescence intensity of blank control as A_{noise}. The SNR of spin-enhanced fluorescence analysis was also calculated using formula 1, with the average intensity fluctuation amplitude of the experimental group as A_{signal} and the average intensity fluctuation amplitude of blank control as A_{noise}. The SNRs of a dilution series of NDs were fitted with a second-order polynomial to derive the concentration-dependent SNR response curve, and the LOD was determined based on a SNR of 3. Detailed methods for LOD calculation are described in "4.12".

4.11. Assay for the AND DLG-QN

The hairpin DNA structure was engineered to implement AND DLG. H1 unfolds its stem-loop structure upon hybridization with miRNA-21, while H2 unfolds upon hybridization with miRNA-155. Subsequent complementary pairing between the two hairpin DNAs occurs only when both miRNA-21 and miRNA-155 are present. In the absence of either miRNA-21 or miRNA-155, at least one of the H1 and H2 remains in its closed conformation, precluding any complementary interaction. Furthermore, ND-H1 and MB-H2 were synthesized to develop AND DLG-QN based on ND fluorescence emission and spin-based modulation. Likewise, the conjugation between ND-H1 and MB-H2 occurs exclusively in the presence of both miRNA-21 and miRNA-155, with a reaction time of 30 min, and purified assemblies are highly enriched by a conical magnet with a sharp tip.

The resulting fluorescence signals from the purified ND-MB assemblies were analyzed using conventional intensity analysis and spin-enhanced analysis (described in "4.9"). The SNR of conventional intensity analysis was calculated using formula 1, with the fluorescence intensity of the experimental group as A_{signal} and the fluorescence intensity of blank control as A_{noise}. The SNR of spin-enhanced fluorescence analysis was also calculated using formula 1, with the average intensity fluctuation amplitude of the experimental group as A_{signal} and the average intensity fluctuation amplitude of blank control as A_{noise}. The SNRs of a dilution series of miRNAs were fitted with a second-order polynomial to derive the concentration-dependent SNR response curve, and the LOD was determined based on a SNR of 3. Detailed methods for LOD calculation are described in "4.12".

4.12. Data Analysis

The SNR was calculated according to the formula listed below[64]

$$\mathrm{SNR} = 20 \times \log_{10}\frac{A_{signal}}{A_{noise}} \tag{1}$$

where A_{signal} is the signal amplitude from detected samples, and A_{noise} is the noise amplitude from blank controls. The LOD was determined based on a SNR of 3.

Thus, the LOD (A_{signal}) was determined according to the formula listed below

$$20 \times \log_{10}\frac{\mathrm{LOD}(A_{signal})}{A_{noise}} = 3 \tag{2}$$

Formula 2 can be converted to the formula listed below

$$\mathrm{LOD}(A_{signal}) = 10^{0.15} \times A_{noise} \tag{3}$$

https://doi.org/10.1021/jacsau.5c00058
JACS Au 2025, 5, 2123−2134

The LOD (concentration) was calculated by converting the LOD (A_{signal}) using the formula obtained from the concentration-dependent SNR response curve.

■ ASSOCIATED CONTENT

Supporting Information

The Supporting Information is available free of charge at https://pubs.acs.org/doi/10.1021/jacsau.5c00058.

Diagram of the developed microwave antenna chip; long-term continuous fluorescence measurement of NDs; PAGE results; SEM images and size distribution plots of ND, ND-H1, BSA-ND-H1, MB, MB-H2, and BSA-MB-H2; SEM image and size distribution plot of ND-MB assemblies; statistical analysis of SNRs calculated from conventional intensity analysis; complete fluorescence images at various combinations of miRNA-21 and miRNA-155 concentrations and the corresponding conventional intensity and spin-enhanced analysis results; flowchart for fabricating a microwave antenna chip; structural parameters of the omega-shaped microwave antenna; diagram of the microwave generating device; comparison of LODs between different oligonucleotide detection methods; and synthesized oligonucleotide sequences (PDF)

■ AUTHOR INFORMATION

Corresponding Authors

Sisi Jia − *Zhangjiang Laboratory, Shanghai 201210, China*; Email: jiass@zjlab.ac.cn

Le Liang − *The Institute for Advanced Studies (IAS), Department of Ophthalmology, Zhongnan Hospital of Wuhan University, State Key Laboratory of Metabolism and Regulation in Complex Organisms, College of Life Sciences, Wuhan University, Wuhan 430072, China*; orcid.org/0000-0001-6682-959X; Email: le.liang@whu.edu.cn

Authors

Weiming Lin − *The Institute for Advanced Studies (IAS), Department of Ophthalmology, Zhongnan Hospital of Wuhan University, State Key Laboratory of Metabolism and Regulation in Complex Organisms, College of Life Sciences, Wuhan University, Wuhan 430072, China*

Tao Ding − *The Institute for Advanced Studies (IAS), Department of Ophthalmology, Zhongnan Hospital of Wuhan University, State Key Laboratory of Metabolism and Regulation in Complex Organisms, College of Life Sciences, Wuhan University, Wuhan 430072, China*

Die He − *Zhangjiang Laboratory, Shanghai 201210, China*

Nan Zhang − *Department of Ophthalmology, Zhongnan Hospital of Wuhan University, Wuhan 430071, China*

Haodong Li − *The Institute for Advanced Studies (IAS), Department of Ophthalmology, Zhongnan Hospital of Wuhan University, State Key Laboratory of Metabolism and Regulation in Complex Organisms, College of Life Sciences, Wuhan University, Wuhan 430072, China*

Wenjian Luo − *The Institute for Advanced Studies (IAS), Department of Ophthalmology, Zhongnan Hospital of Wuhan University, State Key Laboratory of Metabolism and Regulation in Complex Organisms, College of Life Sciences, Wuhan University, Wuhan 430072, China*

Zhongxia Wei − *Zhangjiang Laboratory, Shanghai 201210, China*

Min Ke − *Department of Ophthalmology, Zhongnan Hospital of Wuhan University, Wuhan 430071, China*

Chunhai Fan − *School of Chemistry and Chemical Engineering, New Cornerstone Science Laboratory, Frontiers Science Center for Transformative Molecules, Zhangjiang Institute for Advanced Study and National Center for Translational Medicine, Shanghai Jiao Tong University, Shanghai 200240, China*; orcid.org/0000-0002-7171-7338

Complete contact information is available at: https://pubs.acs.org/10.1021/jacsau.5c00058

Author Contributions

[⊥]W.L. and T.D. contributed equally to this work. The manuscript was written through contributions of all authors. All authors have given approval to the final version of the manuscript.

Notes

The authors declare no competing financial interest.

■ ACKNOWLEDGMENTS

We would like to acknowledge the support from the Start-Up Fund of Wuhan University, the National Natural Science Foundation of China (Grant No. 22374112), and the Translational Medicine and Interdisciplinary Research Joint Fund of Zhongnan Hospital of Wuhan University (Grant No. ZNJC202216). We also thank the Core Facility of Wuhan University for providing access to SEM and DLS instruments.

■ REFERENCES

(1) Yu, S.-J.; Kang, M.-W.; Chang, H.-C.; Chen, K.-M.; Yu, Y.-C. Bright Fluorescent Nanodiamonds: No Photobleaching and Low Cytotoxicity. *J. Am. Chem. Soc.* **2005**, *127*, 17604−17605.

(2) Childress, L.; et al. Coherent Dynamics of Coupled Electron and Nuclear Spin Qubits in Diamond. *Science* **2006**, *314*, 281−285.

(3) Schirhagl, R.; Chang, K.; Loretz, M.; Degen, C. L. Nitrogen-Vacancy Centers in Diamond: Nanoscale Sensors for Physics and Biology. *Annu. Rev. Phys. Chem.* **2014**, *65*, 83−105.

(4) Zheng, P.; Liang, L.; Arora, S.; Ray, K.; Semancik, S.; Barman, I. Pyramidal Hyperbolic Metasurfaces Enhance Spontaneous Emission of Nitrogen-Vacancy Centers in Nanodiamond. *Adv. Opt. Mater.* **2023**, *11*, 2202548.

(5) Du, Z.; Gupta, M.; Xu, F.; Zhang, K.; Zhang, J.; Zhou, Y.; Liu, Y.; Wang, Z.; Wrachtrup, J.; Wong, N.; et al. Widefield Diamond Quantum Sensing with Neuromorphic Vision Sensors. *Advanced Science* **2024**, *11*, 2304355.

(6) Gruber, A.; et al. Scanning Confocal Optical Microscopy and Magnetic Resonance on Single Defect Centers. *Science* **1997**, *276*, 2012−2014.

(7) Balasubramanian, G.; et al. Nanoscale imaging magnetometry with diamond spins under ambient conditions. *Nature* **2008**, *455*, 648−651.

(8) Zhang, T.; Liu, G. Q.; Leong, W. H.; Liu, C. F.; Kwok, M. H.; Ngai, T.; Liu, R. B.; Li, Q. Hybrid nanodiamond quantum sensors enabled by volume phase transitions of hydrogels. *Nat. Commun.* **2018**, *9*, 3188.

(9) Maze, J. R.; et al. Nanoscale magnetic sensing with an individual electronic spin in diamond. *Nature* **2008**, *455*, 644−647.

(10) Hsiao, W. W.-W.; Hui, Y. Y.; Tsai, P.-C.; Chang, H.-C. Fluorescent Nanodiamond: A Versatile Tool for Long-Term Cell Tracking, Super-Resolution Imaging, and Nanoscale Temperature Sensing. *Acc. Chem. Res.* **2016**, *49*, 400−407.

(11) Simpson, D. A.; et al. Non-Neurotoxic Nanodiamond Probes for Intraneuronal Temperature Mapping. *ACS Nano* **2017**, *11*, 12077−12086.

(12) Fujiwara, M.; Sun, S.; Dohms, A.; Nishimura, Y.; Suto, K.; Takezawa, Y.; Oshimi, K.; Zhao, L.; Sadzak, N.; Umehara, Y.; et al. Real-time nanodiamond thermometry probing in vivo thermogenic responses. *Sci. Adv.* **2020**, *6*, No. eaba9636.
(13) Faklaris, O.; et al. Photoluminescent Diamond Nanoparticles for Cell Labeling: Study of the Uptake Mechanism in Mammalian Cells. *ACS Nano* **2009**, *3*, 3955−3962.
(14) Fu, C.-C.; Lee, H. Y.; Chen, K.; Lim, T. S.; Wu, H. Y.; Lin, P. K.; Wei, P. K.; Tsao, P. H.; Chang, H. C.; Fann, W. Characterization and application of single fluorescent nanodiamonds as cellular biomarkers. *Proc. Natl. Acad. Sci. U.S.A.* **2007**, *104*, 727−732.
(15) Waddington, D. E. J.; Sarracanie, M.; Zhang, H.; Salameh, N.; Glenn, D. R.; Rej, E.; Gaebel, T.; Boele, T.; Walsworth, R. L.; Reilly, D. J.; et al. Nanodiamond-enhanced MRI via in situ hyperpolarization. *Nat. Commun.* **2017**, *8*, 15118.
(16) Lazovic, J.; Goering, E.; Wild, A.; Schützendübe, P.; Shiva, A.; Löffler, J.; Winter, G.; Sitti, M. Nanodiamond-Enhanced Magnetic Resonance Imaging. *Adv. Mater.* **2024**, *36*, 2310109.
(17) Miller, B. S.; et al. Spin-enhanced nanodiamond biosensing for ultrasensitive diagnostics. *Nature* **2020**, *587*, 588−593.
(18) Igarashi, R.; et al. Real-Time Background-Free Selective Imaging of Fluorescent Nanodiamonds in Vivo. *Nano Lett.* **2012**, *12*, 5726−5732.
(19) Wu, Y.; Weil, T. Recent Developments of Nanodiamond Quantum Sensors for Biological Applications. *Advanced Science* **2022**, *9*, 2200059.
(20) Aslam, N.; et al. Quantum sensors for biomedical applications. *Nat. Rev. Phys.* **2023**, *5*, 157−169.
(21) Mzyk, A.; Sigaeva, A.; Schirhagl, R. Relaxometry with Nitrogen Vacancy (NV) Centers in Diamond. *Acc. Chem. Res.* **2022**, *55*, 3572−3580.
(22) Li, C.; Soleyman, R.; Kohandel, M.; Cappellaro, P. SARS-CoV-2 Quantum Sensor Based on Nitrogen-Vacancy Centers in Diamond. *Nano Lett.* **2022**, *22*, 43−49.
(23) Mochalin, V. N.; Shenderova, O.; Ho, D.; Gogotsi, Y. The properties and applications of nanodiamonds. *Nat. Nanotechnol.* **2012**, *7*, 11−23.
(24) van der Laan, K.; Hasani, M.; Zheng, T.; Schirhagl, R. Nanodiamonds for In Vivo Applications. *Small* **2018**, *14*, 1703838.
(25) Fan, S.; et al. Quantum Sensing of Free Radical Generation in Mitochondria of Single Heart Muscle Cells during Hypoxia and Reoxygenation. *ACS Nano* **2024**, *18*, 2982−2991.
(26) Xu, F.; Zhang, S.; Ma, L.; Hou, Y.; Li, J.; Denisenko, A.; Li, Z.; Spatz, J.; Wrachtrup, J.; Lei, H.; et al. Quantum-enhanced diamond molecular tension microscopy for quantifying cellular forces. *Sci. Adv.* **2024**, *10*, No. eadi5300.
(27) Chow, E. K.; Zhang, X. Q.; Chen, M.; Lam, R.; Robinson, E.; Huang, H.; Schaffer, D.; Osawa, E.; Goga, A.; Ho, D. Nanodiamond Therapeutic Delivery Agents Mediate Enhanced Chemoresistant Tumor Treatment. *Sci. Transl. Med.* **2011**, *3*, 73ra21.
(28) Yin, F.; Wang, F.; Fan, C.; Zuo, X.; Li, Q. Biosensors based on DNA logic gates. *VIEW* **2021**, *2*, 20200038.
(29) Lin, W.; et al. An integrated sample-to-answer SERS platform for multiplex phenotyping of extracellular vesicles. *Sens. Actuators, B* **2023**, *394*, 134355.
(30) Erbas-Cakmak, S.; et al. Molecular logic gates: the past, present and future. *Chem. Soc. Rev.* **2018**, *47*, 2228−2248.
(31) Qu, X.; et al. Programming Cell Adhesion for On-Chip Sequential Boolean Logic Functions. *J. Am. Chem. Soc.* **2017**, *139*, 10176−10179.
(32) Wang, F.; Lv, H.; Li, Q.; Li, J.; Zhang, X.; Shi, J.; Wang, L.; Fan, C. Implementing digital computing with DNA-based switching circuits. *Nat. Commun.* **2020**, *11*, 121.
(33) Okamoto, A.; Tanaka, K.; Saito, I. DNA Logic Gates. *J. Am. Chem. Soc.* **2004**, *126*, 9458−9463.
(34) Dong, J.; Wang, M.; Zhou, Y.; Zhou, C.; Wang, Q. DNA-Based Adaptive Plasmonic Logic Gates. *Angew. Chem., Int. Ed.* **2020**, *59*, 15038−15042.
(35) Lv, H.; et al. DNA-based programmable gate arrays for general-purpose DNA computing. *Nature* **2023**, *622*, 292−300.
(36) Lund, K.; et al. Molecular robots guided by prescriptive landscapes. *Nature* **2010**, *465*, 206−210.
(37) Ouyang, Y.; Zhang, P.; Willner, I. DNA Tetrahedra as Functional Nanostructures: From Basic Principles to Applications. *Angew. Chem., Int. Ed.* **2024**, *63*, No. e202411118.
(38) Li, M.; et al. DNA Framework-Programmed Cell Capture via Topology-Engineered Receptor−Ligand Interactions. *J. Am. Chem. Soc.* **2019**, *141*, 18910−18915.
(39) Song, S.; et al. Functional nanoprobes for ultrasensitive detection of biomolecules. *Chem. Soc. Rev.* **2010**, *39*, 4234−4243.
(40) Giovanni, M.; et al. Electrochemical Quantification of Escherichia coli with DNA Nanostructure. *Adv. Funct. Mater.* **2015**, *25*, 3840−3846.
(41) Tian, Z.; et al. Aptamer-Braked Multi-hairpin Cascade Circuits for Logic-Controlled Label-Free In Situ Bioimaging. *Anal. Chem.* **2020**, *92*, 10357−10364.
(42) Liang, L.; Jia, S.; Barman, I. DNA-POINT: DNA Patterning of Optical Imprint for Nanomaterials Topography. *ACS Appl. Mater. Interfaces* **2022**, *14*, 38388−38397.
(43) Liang, L.; et al. DNA-Patched Nanoparticles for the Self-Assembly of Colloidal Metamaterials. *JACS Au* **2023**, *3*, 1176−1184.
(44) Liang, L.; Zheng, P.; Zhang, C.; Barman, I. A Programmable DNA-Silicification-Based Nanocavity for Single-Molecule Plasmonic Sensing. *Adv. Mater.* **2021**, *33*, 2005133.
(45) Sharma, J.; et al. Control of Self-Assembly of DNA Tubules Through Integration of Gold Nanoparticles. *Science* **2009**, *323*, 112−116.
(46) Saghatelian, A.; Völcker, N. H.; Guckian, K. M.; Lin, V. S. Y.; Ghadiri, M. R. DNA-Based Photonic Logic Gates: AND, NAND, and INHIBIT. *J. Am. Chem. Soc.* **2003**, *125*, 346−347.
(47) Pei, H.; et al. Reconfigurable Three-Dimensional DNA Nanostructures for the Construction of Intracellular Logic Sensors. *Angew. Chem., Int. Ed.* **2012**, *51*, 9020−9024.
(48) Dong, H.; et al. MicroRNA: Function, Detection, and Bioanalysis. *Chem. Rev.* **2013**, *113*, 6207−6233.
(49) Endzeliņš, E.; Melne, V.; Kalniņa, Z.; Lietuvietis, V.; Riekstiņa, U.; Llorente, A.; Linē, A. Diagnostic, prognostic and predictive value of cell-free miRNAs in prostate cancer: a systematic review. *Mol. Cancer* **2016**, *15*, 41.
(50) Nakamura, K.; Sawada, K.; Yoshimura, A.; Kinose, Y.; Nakatsuka, E.; Kimura, T. Clinical relevance of circulating cell-free microRNAs in ovarian cancer. *Mol. Cancer* **2016**, *15*, 48.
(51) Yang, J.; et al. Early screening and diagnosis strategies of pancreatic cancer: a comprehensive review. *Cancer Commun.* **2021**, *41*, 1257−1274.
(52) Ye, L.; Yang, F.; Ding, Y.; Yu, H.; Yuan, L.; Dai, Q.; Sun, Y.; Wu, X.; Xiang, Y.; Zhang, G. Bioinspired Trans-Scale Functional Interface for Enhanced Enzymatic Dynamics and Ultrasensitive Detection of microRNA. *Adv. Funct. Mater.* **2018**, *28*, 1706981.
(53) Yang, Y.; Lu, H.; Fang, D.; Zhang, Y.; Tang, Y.; Zhao, S.; Yan, J.; Qin, X.; Shen, J.; Yang, F. DNA-encoded plasmonic bubbles aggregating dual-microRNA SERS signals for cancer diagnosis. *Aggregate* **2024**, *5*, No. e636.
(54) Tang, Y.; Xiang, Y.; Yang, Y.; Zhang, Y.; Wei, B.; Qin, X.; Fang, M.; Wang, Q.; Li, X.; Yang, F. Nanostructured Bubbles-Enhanced Fluorescence for Ultrasensitive Portable MicroRNA Detection. *Adv. Funct. Mater.* **2025**, *35*, 2413832.
(55) Feng, C.; et al. Construction of a Ternary Complex Based DNA Logic Nanomachine for a Highly Accurate Imaging Analysis of Cancer Cells. *ACS Sens.* **2020**, *5*, 3116−3123.
(56) Wang, D.; Li, S.; Zhao, Z.; Zhang, X.; Tan, W. Engineering a Second-Order DNA Logic-Gated Nanorobot to Sense and Release on Live Cell Membranes for Multiplexed Diagnosis and Synergistic Therapy. *Angew. Chem., Int. Ed.* **2021**, *60*, 15816−15820.
(57) Chen, B.; et al. Cell Membrane-Anchored AND Logic Gate Aptasensor for Tumor Cell-Specific Imaging with Improved Accuracy. *Anal. Chem.* **2024**, *96*, 14775−14782.

https://doi.org/10.1021/jacsau.5c00058
JACS Au 2025, 5, 2123−2134

(58) Wang, F.; et al. Paper-based closed Au-Bipolar electrode electrochemiluminescence sensing platform for the detection of miRNA-155. *Biosens. Bioelectron.* **2020**, *150*, 111917.
(59) Xu, J.; Qiu, X.; Hildebrandt, N. When Nanoworlds Collide: Implementing DNA Amplification, Nanoparticles, Molecules, and FRET into a Single MicroRNA Biosensor. *Nano Lett.* **2021**, *21*, 4802−4808.
(60) Wang, J. J.; et al. The exploration of quantum dot-molecular beacon based MoS2 fluorescence probing for myeloma-related Mirnas detection. *Bioact. Mater.* **2022**, *17*, 360−368.
(61) Tan, H.-S.; Wang, T.; Han, J.-M.; Liu, M.; Li, S.-S. Dual-signal SERS biosensor based on spindle-shaped gold array for sensitive and accurate detection of miRNA 21. *Sens. Actuators, B* **2024**, *403*, 135157.
(62) Chen, F.-Z.; Hou, L.; Gao, Y.; Zhou, J.; Kong, F.; Han, D.; Zhao, W. Polyoxometalates: Cascading Functionality to Unique On-Off Organic Photoelectrochemical Transistor Operation. *Adv. Funct. Mater.* **2024**, *34*, 2408186.
(63) Wang, W.; et al. AI-Enhanced Visual-Spectral Synergy for Fast and Ultrasensitive Biodetection of Breast Cancer-Related miRNAs. *ACS Nano* **2024**, *18*, 6266−6275.
(64) Sheen, H.-J.; et al. Electrochemical biosensor with electro-kinetics-assisted molecular trapping for enhancing C-reactive protein detection. *Biosens. Bioelectron.* **2022**, *210*, 114338.

https://doi.org/10.1021/jacsau.5c00058
JACS Au 2025, 5, 2123−2134